FEA-Augmented Design Equations for Synchronous Reluctance Machines

FEA-Augmented Design Equations for Synchronous Reluctance Machines

Simone Ferrari, *Student Member, IEEE* and Gianmario Pellegrino, *Senior Member, IEEE*
Department of Energy "*Galileo Ferraris*"
Politecnico di Torino, Turin, Italy
Email: simone.ferrari@polito.it, gianmario.pellegrino@polito.it

***Abstract*—The synchronous reluctance machine is an attractive substitute of induction motors and synchronous PM motors thanks to its higher efficiency and lower cost of materials, respectively. One of the main challenges relenting the adoption of these machines is the lack of a widely recognized procedure for their design. In the past, design equations were proposed for SyR machines by different authors. Those models represent a good starting point and a useful guideline for the designer, but they are far from being accurate enough in many aspects. To increase precision, different procedures based on finite element analysis were proposed over the years, but those methods have the dual downside of losing the physical insight on the effect of the various design parameters. In this work, a comprehensive design procedure based on design equations is reviewed and improved using few static FEA simulations to fix the errors of the analytical model, in order to increase the precision without reducing the generality of the model.**

I. Introduction

Synchronous Reluctance (SyR) machines were proposed in the last years as a cost competitive and efficient alternative to other kind of machines in many fields of application. Compared to Surface-mounted Permanent Magnet (SPM) machines, the SyR machine solution can reduce cost and increase safety at high-speed operations, thanks to the absence of rare-earth Permanent Magnets (PMs). These advantages are balanced by a more complex design procedure, lower power and energy density, and a more complicated control strategy. Against Induction Machines (IMs), SyR machines exhibit higher efficiency, due to the absence of rotor cage loss, and similar if not lower manufacturing cost. On the other hand, IMs have in general a better power factor and well established design procedures.

The literature reports different approaches to the design of SyR machines. Examples of use of pure analytical models are in [1], [2] and [3]. These methods are general and allow a good understanding of the machine behavior, but they are not very precise in terms of performance figures estimation. The second approach includes all the methods based on Finite Elements Analysis (FEA), as [4] and [5]. Their precision is high, but very often the design process heavily relies on optimization algorithms, which limit the generality of the results and narrow the insight of the designer on the results he obtains. Besides the precision and the designer insights, a substantial difference between the two approaches is the computational time. Analytical models takes up to some seconds to evaluate several machine model, while FEA-based approaches needs up to some minutes to evaluate one model.

This paper introduces a new design procedure that joins the benefits of the analytical and FEA approaches: the design equations are refined by fast FEA simulations, used to correct the equations and not to evaluate the output figure of a specific design. This hybridized design process ensures both generality and short computational time, typical of the analytical models, with augmented precision given by the FEA simulations. The contributions of this paper are:

- to review the design literature of SyR machines;
- to improve the design equations by including the effect of saturation on the magnetizing current;
- to include the cross saturation effect into the model by way of selected FEA simulations.

All the procedures and the equations presented in the paper are embedded SyR-e [11], an open-source tool for electrical machines design.

II. Review of the Analytical Model

The magnetic model of a SyR machine, represented in the dq frame, can be written as:

$$\begin{cases} \lambda_d = (L_{md} + L_\sigma)\, i_d \\ \lambda_q = (L_{mq} + L_\sigma)\, i_q \end{cases} \tag{1}$$

where λ_d and λ_q are the d- and q-axis flux linkages, and i_d and i_q are the dq current components. L_{md} and L_{mq} are the respective magnetizing components and L_σ is the leakage inductance. All the inductances depend on geometric inputs, as the stator outer radius R, the stack length L, the airgap length g, the stator slot size, the flux barriers shape and position. Moreover, two per-unit parameters will be used, as explained later. Current loading can be indirectly imposed through the thermal loading factor k_j (2), expressed as the ratio between the allowed copper loss and the stator outer surface:

$$k_j = \frac{\frac{3}{2} R_s\, i_0^2}{2\pi R L} = \frac{(6\, N_s\, i_0)^2}{\frac{k_{Cu}}{\rho}\, \frac{L}{L+l_{end}}\, 4\, \pi\, R\, A_{slots}} \tag{2}$$

where i_0 is the thermal rated current, considered the number of turns in series per phase N_s. The term k_{Cu} represents the slot filling factor, ρ is the copper resistivity, l_{end} is the end-winding length and A_{slots} is the total cross-section of the slots (sum of all slots). The thermal loading factor k_j accounts for the

cooling system during the design process, thanks to its easy definition. Typical values are $k_j = 1.5 \sim 3\,kW/m^2$ for self-ventilated machines, $k_j = 5 \sim 12\,kW/m^2$ for machines with forced ventilation and $k_j = 12 \sim 20\,kW/m^2$ for water-cooled machines.

A. Per-unit factors

According to [6], two per-unit factor are used in the model definition. They are the rotor/stator split ratio x (3) and the airgap/iron flux density ratio b (4).

$$x = \frac{r}{R} \tag{3}$$

$$b = \frac{B_g}{B_{Fe}} \tag{4}$$

where r and R are the rotor and stator outer radii, respectively. B_{Fe} is the peak flux density in the stator yoke and B_g is the peak flux density in the airgap. These two factors will be used in a parametric study, enabling the evaluation of several designs with a limited computational effort and linking the geometrical definitions with the machine outputs.

B. Torque equation

The general torque equation, valid for SyR machine is:

$$T = \frac{3}{2}\,p\,(\lambda_d\,i_q - \lambda_q\,i_d) \tag{5}$$

where p is the number of pole pairs. Substituting (1) in (5) it results in:

$$T = \frac{3}{2}\,p\,(L_{md} - L_{mq})\,i_d\,i_q \tag{6}$$

This easy substitution highlights an important property: the leakage inductance does not affect the output torque. Manipulating (6), it follows:

$$T = \frac{3}{2}\,p\,k_{dq}\,\lambda_{md}\,i_q \tag{7}$$

$$k_{dq} = 1 - \frac{L_{mq}}{L_{md}} \tag{8}$$

where k_{dq}, defined in (8), accounts for saliency and derives mainly from rotor design. The term $\lambda_{md} = L_{md}\,i_d$ stands for the magnetizing flux linkage. The q-axis current is obtained as $i_q = \sqrt{i_0^2 - i_d^2}$, where i_0 derives from k_j according to (2) and i_d is the current component producing λ_{md}.

C. Stator design and d-axis equations

The magnetizing flux linkage λ_{md} is computed through the main dimensions of the machine and the iron flux density:

$$\lambda_{md} = \frac{2\,R\,L\,k_w\,N_s}{p}\,B_{Fe}\,x\,b \tag{9}$$

where k_w is the winding factor. The magnetizing current necessary to create the target flux linkage is:

$$i_d = \frac{\pi\,k_c\,g\,p}{3\,\mu_0\,k_w\,N_s}\,B_{Fe}\,b \tag{10}$$

where k_c is the Carter's coefficient. As addressed previously, all the quantity are expressed as a function of the two per-unit

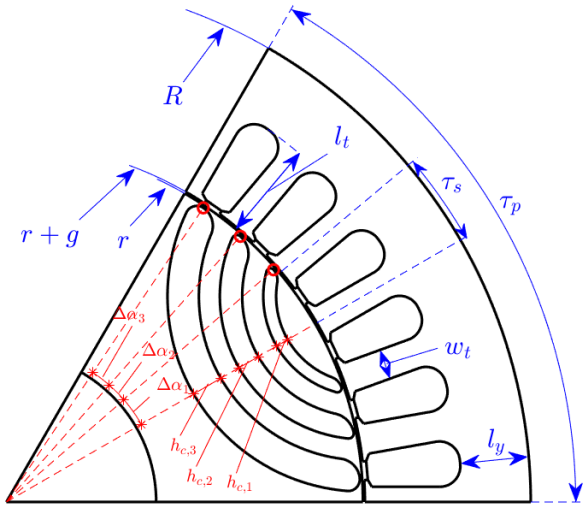

Fig. 1. Main dimension of a general SyR machine

parameters x and b. The d-axis magnetizing inductance can be easily evaluated as the ratio between (9) and (10). L_{md} will be used as the base value for all the others inductances estimation.

$$L_{md} = \frac{\lambda_{md}}{i_d} \tag{11}$$

Once the d-axis flux linkage and the flux density levels are defined, it is possible to compute the main stator dimensions: the yoke length l_y (12) and the tooth width w_t (13). An oversizing of these parameters could lead to a low exploitation of the material limits, while an undersizing could cause deep saturation of the iron, with a performance deterioration. Ideally, the yoke length shall permit the flow of half the flux in the pole pitch. Setting the peak flux density in the yoke equal to B_{Fe}, it follows:

$$l_y = \frac{R}{p}xb \tag{12}$$

Concerning the tooth sizing, the tooth width must allow the flow of the maximum flux linkage in one slot pitch. In this case, a tooth reduction factor can be introduced to deform the B_g waveform and increase its the fundamental amplitude. The tooth width results in:

$$w_t = \frac{2\pi R}{6pq}k_t\,xb \tag{13}$$

where q is the number of slots per pole per phase and k_t is the tooth reduction factor. If $k_t = 1$, the peak tooth flux density is equal to B_{Fe}, while if $k_t < 1$, the peak tooth flux density increase, ideally up to B_{Fe}/k_t if an unsaturated iron model is used. Fig. 1 reports in blue the main stator dimension.

D. Rotor design and q-axis equations

The q-axis design mainly deals with the rotor geometry, and principally with the flux barriers design. The magnetizing inductance L_{mq} can be divided into two fundamental terms: the circulating term L_{cq} and the flow-through term L_{fq}. The

former models all the flux linkage paths that cross the airgap, but not the rotor, while the latter account for the flux linkage that cross the rotor and the flux barriers along the q-axis. The circulating component can be evaluated as [6]:

$$\frac{L_{cq}}{L_{md}} = 1 - \frac{4}{\pi} \sum_k f_k^2 \, \Delta\alpha_k \tag{14}$$

where f_k is the stator Magneto-Motive Force (MMF) applied to the k^{th} flux barrier and $\Delta\alpha_k$ is the flux barrier position along the airgap. As mentioned previously, the inductance is written in per-unit value, referred to L_{md}. The inductance L_{cq} is affected by the rotor layer number and position, that are designed starting from the number of stator slots. Assumed a number of stator slots per pole pair $n_s = 6q$, the number of equivalent rotor slots per pole pair should be $n_r = n_s \pm 4$. This combination is a trade-off between the torque ripple minimization and the iron loss reduction, as addressed in [8]. The flow-through component L_{fq} can be estimated with [6]:

$$\frac{L_{fq}}{L_{md}} = \frac{4}{\pi} \frac{p \, k_c \, g}{R \, x} \sum_k f_k^2 \frac{s_k}{h_{c,k}} \tag{15}$$

where s_k is the flux barrier length (in the d-axis direction) and h_c is the flux barrier width (q-axis direction). This inductance is mainly affected by the flux barriers width: thicker is the barriers, lower is L_{fq}. Moreover, thick barriers means thin flux carriers, that can saturate, increasing the magnetizing current needed to reach the target flux linkage. To avoid premature rotor iron saturation, the total flux carrier width must be at least equal to the stator yoke l_y, limiting the total barrier width. About the single $h_{c,k}$, different rules can be used. The suggestion given in [6] is to set constant barrier permeance. This ratio reduces the torque ripple if the machine is complete [1], and limits the problems of local demagnetization if permanent magnets are inserted in the flux barrier. Moreover, constant barrier permeance rule can lead to thin flux carriers, that will saturate. A further degree of freedom in the flux barrier definition (called Δx) is added, according to [9]. This parameter admits the flux barriers move along the q-axis, as shown in Fig. 2. In this picture, the blue lines represent the barriers axes, defined by $\Delta\alpha$, and Δx is constant to each flux barriers. The picture highlight that Δx does not affect the position of the flux barriers along the airgap, and so the number of rotor slots. Furthermore, Δx permits to design the rotor in order to have constant flux carrier width and avoid unwanted local saturations.

E. Rotor ribs effect

The flow-through component models the flux carriers as disconnected one from the others. In real machines, iron ribs connect the flux carriers along the q-axis, to make the rotor mechanically feasible. This iron ribs act like magnetic short-circuit, providing a preferential path for flux lines along the q-axis. The related flux linkage is limited by the ribs iron saturation and their small dimension. Furthermore, to have an accurate estimation, an additional L_{mq} component must be introduced. According to [6], the rotor ribs inductance L_{rq}

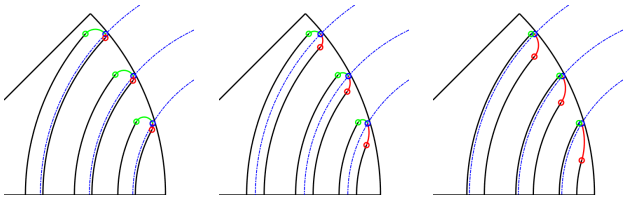

Fig. 2. Effect of Δx on rotor flux barriers: $\Delta x = -1$ (a), $\Delta x = 0$ (b) and $\Delta x = +1$ (c). Blue lines reports the barriers axes

can be evaluated setting a given flux density B_{ribs} in the ribs, from the saturated region of the iron characteristic.

$$L_{rq} = \frac{4}{\pi} \, k_w \, N_s \, w_{ribs} \, l \, \frac{B_{ribs}}{i_q} \tag{16}$$

where w_{ribs} is the total ribs width in the flux barrier.

F. Power factor equation and slot leakage inductance

The power factor $cos\varphi$ is another important performance figure of SyR machines. If the motor is not well-designed, power factor can be low, increasing the inverter size. Neglecting the phase resistance, the power factor can be evaluated as:

$$cos\varphi = sin(\gamma - \delta) \tag{17}$$

where γ and δ are the current and flux linkage angles respectively, both evaluated starting from the d-axis. The leakage inductance affects the power factor, but its influence is not clear from (17). Manipulations of (17) lead to complicate and less intuitive equations. To highlight the L_σ effect, the maximum power factor equation (18), introduced in [7], can be used:

$$cos\varphi_{max} = \frac{L_d - L_q}{L_d + L_q} = \frac{L_{md} - L_{mq}}{L_{md} + L_{mq} + 2\,L_\sigma} \tag{18}$$

Substituting (8) in (18), it follows:

$$cos\varphi_{max} = \frac{k_{dq}}{2 - k_{dq} - \frac{L_\sigma}{L_{md}}} \tag{19}$$

The first parameter affecting the power factor is the anisotropy. For a poor anisotropy machine ($k_{dq} << 1$), the power factor will be low, even neglecting the leakage effect ($L_\sigma = 0$). This behavior is in accordance with the need to have high anisotropy ($k_{dq} \simeq 1$) for the torque purpose. The other parameter that reduce the power factor is the leakage inductance L_σ, as said before. This inductance depends on the slot size: bigger the slot, higher L_σ and lower the power factor. According to [6], the leakage inductance can be evaluated as:

$$\frac{L_\sigma}{L_{md}} = \frac{4}{\pi} \, p \, \frac{k_c \, g}{R \, x} \, p_s \sum_k \Delta f_{s,k}^2 \tag{20}$$

where $\Delta f_{s,k}$ are the stator MMF staircase in pu, and p_s is a permeance factor of the stator slot, evaluated as:

$$p_s = \frac{d_0}{c_0} + \frac{d_1}{c_0} \frac{1}{\frac{c_1}{c_0} - 1} \, ln\left(\frac{c_1}{c_0}\right) + \frac{d_2}{c_2} \, h \tag{21}$$

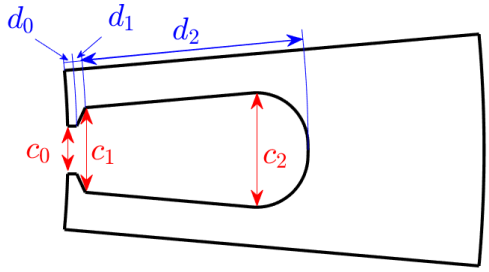

Fig. 3. Stator slot dimensions for leakage inductance evaluation

TABLE I
DESIGN PROCESS INPUTS

Number of pole pairs	p	3
Number of slots per pole per phase	q	2
Stator outer radius $[mm]$	R	87.5
Stack length $[mm]$	L	110
Airgap length $[mm]$	g	0.325
Iron flux density $[T]$	B_{Fe}	1.4
Thermal loading factor $[kW/m^2]$	k_j	2.8
Tooth width factor	k_t	0.89
Number of turns in series per phase	N_s	108

where h is defined in (22) and the other parameters are the dimensions defined in Fig. 3.

$$h = \frac{\beta^2 - \frac{\beta^4}{4} - ln(\beta) - \frac{3}{4}}{(1-\beta)(1-\beta^2)^2} \tag{22}$$

with $\beta = c_1/c_2$.

III. PARAMETRIC DESIGN PLANE $T(x,b) - cos\varphi(x,b)$

The core of the analytical design process presented in [6] is the parametric design plane. On this plot, torque and power factor are reported as a function of the two per-unit factor x and b, defined previously. Each point of the xb-plane correspond to a different machine, according to the design rules and equation introduced in this section. Table I reports the inputs of the design process, with reference of an existing SyR machine [10]. The input set contain both geometric characteristic (R, L, g, p, q, k_t) and design constraints as the target flux density in the iron B_{Fe} and the thermal loading k_j.

Fig. 4 shows the design plane obtained from the data reported in Table I. The torque contours (7) are plotted in red, while the power factor contours (17) are reported in blue. Three machines are designed starting from this plane, and are reported in Fig. 5. They are:

- **Mot1**: same stator of the IM presented in [10]. $x = 0.68$ and $b = 0.55$
- **Mot2**: highlights the effect of x variations. $x = 0.58$ and $b = 0.55$
- **Mot3**: highlights the effect of b variations. $x = 0.68$ and $b = 0.45$

Starting from Mot1, the x reduction leads to an increase of the slot area, resulting in higher output torque. The slot area growth causes also a $cos\varphi_{max}$ reduction. Power factor curves

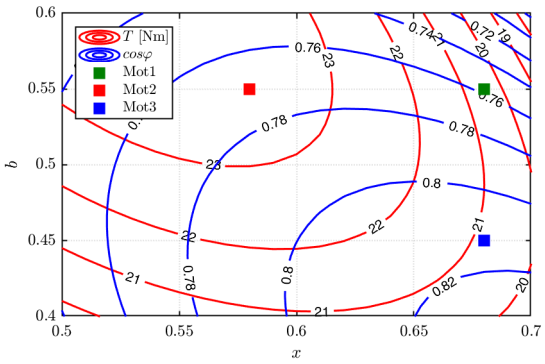

Fig. 4. Parametric design plane obtained with the analytical model: Torque (red contours) and power factor (blue contours) function of x and b

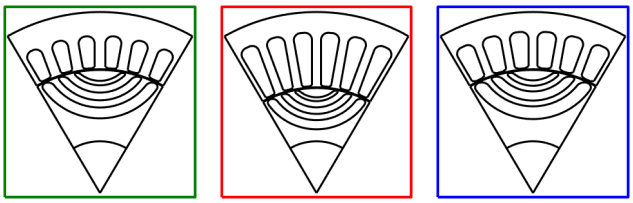

(a) (b) (c)

Fig. 5. Design examples from the xb-plane: Mot1 (a), Mot2 (b) and Mot3(c)

do not reflect this trend because of the working point change. The current angle γ grows with the x reduction, increasing $cos\varphi$ up to its maximum value. About b reductions, the trend is opposite because L_{fq} heavily decreases with the flux barrier width increase. The effect on torque is less evident because the reduced flux linkage tends to reduce torque, while the higher q-axis current (caused by an increase of the slot area and a decrease of the magnetizing current) tends to keep the torque high. On the contrary, the b reduction increase the $cos\varphi_{max}$ thanks to the higher anisotropy. As in the previous, the trend on $cos\varphi$ is slightly different because of the different current angle.

A. Preliminary FEA validation

To verify the accuracy of the analytical model, the whole design domain is analyzed with FEA simulations. Fig. 6 reports the FEA results of torque (Fig. 6a) and power factor (Fig. 6b) with dashed lines, while the analytical model estimation are reported with solid contours. The different contour colors highlight the different values of the performance figure. The discrepancy between the analytical model and the FEA validation is evident: the torque difference is around 5 Nm, while the $cos\varphi$ gap is 0.04 circa. Furthermore, also the contour shape of the analytical model is slightly different of the FEA simulations contours, attesting a model error.

B. Model refinements

In this section, the refinements on the analytical model are presented. The main behaviors neglected in the analytical model (from now addressed as 'initial model') are the iron

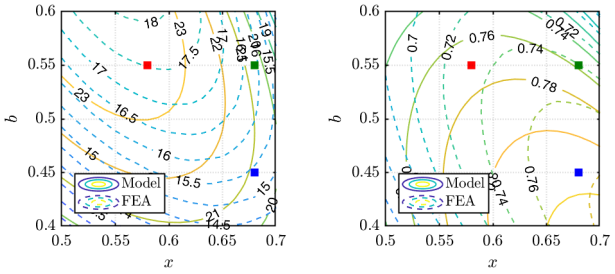

(a) (b)

Fig. 6. Comparison between the initial model estimation (solid lines) and the FEA simulation (dashed lines) of torque (a) and power factor (b) evaluated in the working point defined by the loading factors.

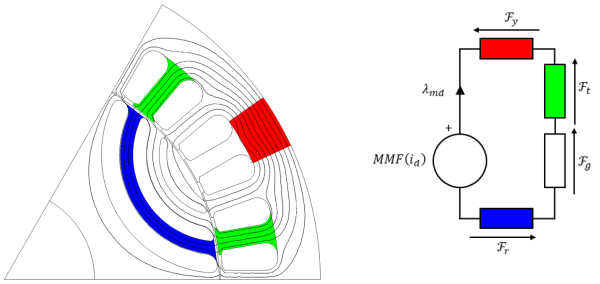

(a) (b)

Fig. 7. Iron section added to the d-axis model for the saturation factor computation (a) and equivalent circuit (b)

MMF drops along the d-axis and the cross-saturation. Some analytical models exist for the former effect but they rely on complex calculations and different iterations to keep into account the non-linear iron characteristic. The latter effect is hard to formalize and the existing methods are not precise. The solution proposed in this paper is to correct the flux linkage model (1) with three factors as reported in (23). The factor k_{sat} accounts for the iron saturation along the d-axis, and it is evaluated with a trivial analytical model, while $k_{cross,d}$ and $k_{cross,q}$ are correction factors used to model the cross-saturation effect. If all the added factors are equal to one, the model is equal to the initial model.

$$\begin{cases} \lambda_d = k_{cross,d}\,(\frac{L_{md}}{k_{sat}} + L_\sigma)\,i_d \\ \lambda_q = k_{cross,q}\,(L_{mq} + L_\sigma)\,i_q \end{cases} \tag{23}$$

C. Saturation factor k_{sat}

The initial model accounts only for the MMF drop along the airgap, neglecting the iron path drops. Ideally, the iron relative permeability μ_{Fe} is much higher than the air permeability, and the omission is acceptable. Moreover, if the iron is near or over its saturation level, the relative permeability drastically fall down, increasing the iron MMF drop. An accurate model of the stator iron should take into account the contribution of all the tooth, in different load conditions, and the whole yoke, with not constant flux density. This kind of approach is based on heavy calculations, that increase the computational time of the process, without having a huge advantage in terms of precision. The easier solution, adopted here, is to accounts only for the most loaded parts of the machine. This approach is quite precise, because the main MMF drops happen in this iron sections. Furthermore, no iterative loops are needed because the flux density in this regions is imposed as design input. Fig. 7a shows the considered part on the machine geometry. They are:

- Two stator teeth (length equal to $2\,l_t$), shown in green
- The section of the stator yoke between two teeth (length equal to $l_{sat,s} = \frac{\pi}{3pq}(R - \frac{l_y}{2})$), highlighted in red
- The inner rotor flux carrier (length equal to $l_{sat,r}$), colored in blue

The equivalent circuit of the d-axis is reported in Fig. 7b. The added part are the colored one, with the same colors as the highlighted sections on the machine lamination. The saturation factor k_{sat} is evaluated according to (24)

$$k_{sat} = 1 + \frac{\mathcal{F}_y + \mathcal{F}_t + \mathcal{F}_r}{\mathcal{F}_g} \tag{24}$$

where the therms $\mathcal{F}$ represents the MMF drops in the magnetic equivalent circuit according to Fig. 7b. They are evaluated starting from the sizes of the colored areas of Fig. 7a and the flux density inputs:

$$\mathcal{F}_y = H_y\,l_{sat,s} = H(B_{Fe})\,\frac{\pi}{3pq}(R - \frac{l_y}{2}) \tag{25}$$

$$\mathcal{F}_t = H_t\,2\,l_t = H(B_{Fe}/k_t)\,2\,l_t \tag{26}$$

$$\mathcal{F}_r = H_r\,l_{sat,r} = H(B_{Fe})\,l_{sat,r} \tag{27}$$

$$\mathcal{F}_g = \frac{b\,B_{Fe}}{\mu_0}\,k_c\,g \tag{28}$$

The saturation factor is multiplied to the magnetizing current i_d in order to increase it and reach the target flux linkage, while the d-axis magnetizing inductance is re-computed with the correct d-axis current. The results are:

- an increase of the magnetizing current needed to reach the target flux density
- a reduction of the d-axis magnetizing inductance.

The former effect change the design working point, while the latter affects the magnetic model, only on the d-axis. The base value for L_{mq} computation is not updated with the saturation factor. Fig. 8 shows the k_{sat} values of the case study presented in the previous section. The saturation effect increase with the reduction of the two design parameters. The x decrease causes a rise of l_t, and so, the MMF tooth drop, while the b reduction causes a shrinking of the yoke length, that increase the tooth length, and so the MMF tooth drop. An interesting insight of this upgrade can be highlight by comparing Fig. 6 and Fig. 8. The k_{sat} value is high where the FEA-model discrepancy is high, while is closer to one where the discrepancy is lower. This feature allows to change the contour shape of the performance figures, making them closer to the FEA results.

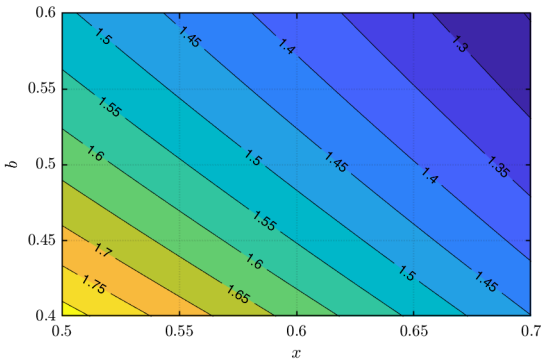

Fig. 8. Saturation factor values for the case study in Table I

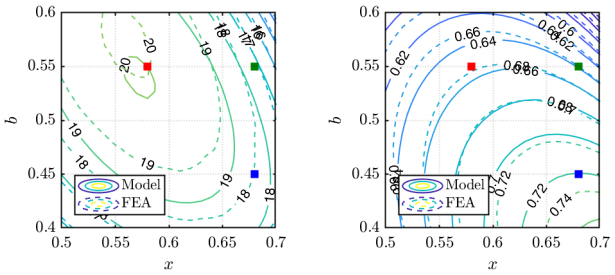

(a) (b)

Fig. 9. Comparison between the analytical model with saturation factor (solid lines) and the FEA simulations (dashed lines) on torque (a) and power factor (b)

Fig. 9 reports the results of this upgrade. In the two plots, the torque (Fig. 9a) and the power factor (Fig. 9b) contours are reported. The results of the upgraded analytical model are plotted in solid lines, while the FEA results are plotted with dashed lines. The improvement is evident: the contours shape of the saturated model is close to the FEA contours. Moreover, a limited discrepancy between model and FEA still exists in some areas of the plane.

D. Fast FEA fix of cross-saturation error (FEAfix)

The cross-saturation effect is the reduction of one flux linkage term due to the current on the other axis. This behavior is neglect in the initial model and analytical expressions to compute the cross-saturation are difficult to define and not always accurate. Moreover, the proposed solution is to model the cross-saturation using two coefficient (one for each axis) multiplied for the flux linkages obtained by the analytical model, as reported in (23). This two factors (named $k_{cross,d}$ and $k_{cross,q}$) are computed with fast FEA simulations of selected machines on the xb-plane. They are evaluated as:

$$k_{cross,d} = \frac{\lambda_{d,FEA}}{\left(\frac{L_{md}}{k_{sat}} + L_\sigma\right) i_d} \tag{29}$$

$$k_{cross,q} = \frac{\lambda_{q,FEA}}{\left(L_{mq} + L_\sigma\right) i_q} \tag{30}$$

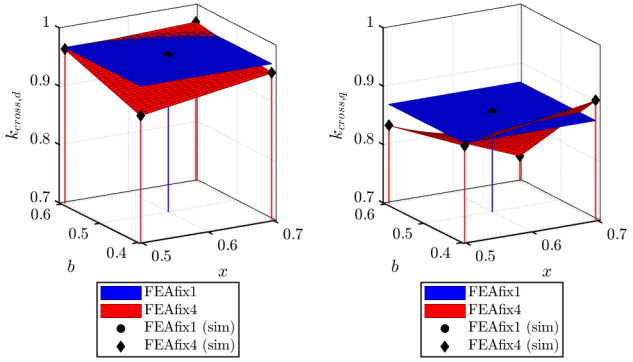

(a) (b)

Fig. 10. Cross-saturation factors $k_{cross,d}$ (a) and $k_{cross,q}$ (b) over the x, b plane. Blue: using 1 FEA simulation (FEAfix1 - black dot). Red: using4 FEA simulations (FEAfix4 - black diamonds).

where the subscript *FEA* point out the FEA results. Ideally, the whole design domain can be FEA evaluated to have precise estimations, but the speed advantage given by the analytical approach will be lost. The proposed solution is to select only few significant points of the design domain for the FEA-calibration, and then extend the factors obtained to the full design domain. The first solution, called FEAfix1 computes $k_{cross,d}$ and $k_{cross,q}$ only in the center of the design domain, and use this value in the full (x, b) range. A more precise and computing-expensive solution is called FEAfix4 and relies on the FEA evaluation of the four machines at the corners of the design domain. The factors locally obtained are then extended to the full xb-plane using linear interpolation. Fig. 10 shows the correction factors in the xb-plane computed for the case study. The blue surfaces are the FEAfix1 results, while FEAfix4 results are reported in red. According to the definition, the FEAfix1 coefficients are constant in the whole xb domain, and their values correspond to the FEA results in the central point (black circle). The results using FEAfix4 are more complex: the red surfaces are obtained using linear interpolation between the four FEA-evaluated points, tagged with black diamonds. The cross-saturation factors are always lower than one, as expected. In general, $k_{cross,q}$ is lower than $k_{cross,d}$ because the q-axis flux linkage is lower and the relative effect of the cross saturation is higher. The cross saturation correction factors are related to the dual currents: $k_{cross,d}$ has a similar shape of $-i_q$, while $k_{cross,q}$ shape is similar to $-i_d$ surface. This is reasonable and holds with the definition of cross-saturation: higher the current on the other axis, lower the flux linkage on the considered axis. The validation process with the entire xb-plane evaluated with FEA simulations confirms the benefits of the FEAfix procedure. Fig. 11 shows the comparison between FEAfix models and full FEA simulations. Thanks to the minimal FEA approach, the model contours and the FEA contours are quite superimposed. The maximum accuracy is reached, obliviously, near the FEAfix simulations points, tagged in black in Fig. 11.

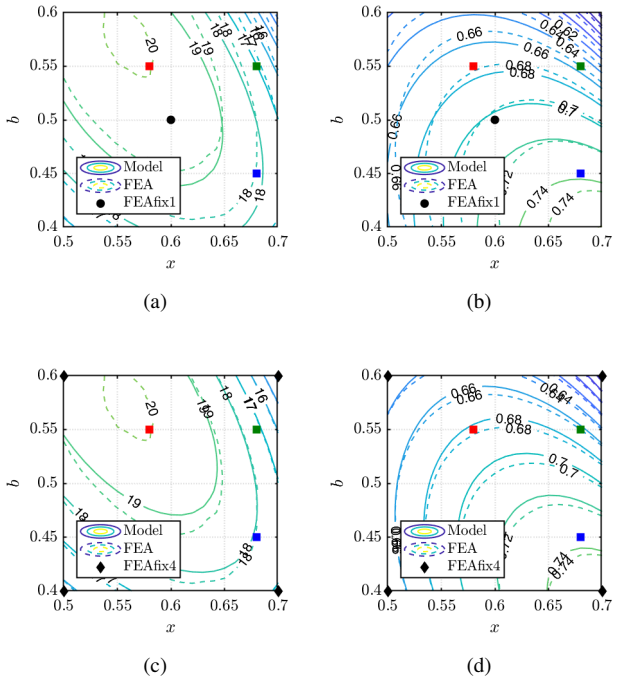

Fig. 11. Comparison between the performance figures estimated with the FEAfix models and the FEA validation. Torque (a) and power factor (b) of FEAfix1 model and torque (c) and power factor (d) of FEAfix4 model.

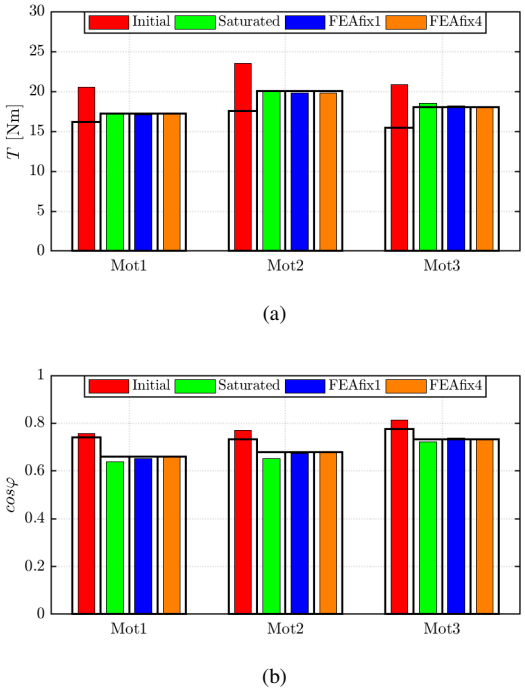

Fig. 12. Comparison between the analytical models and FEA results for the three benchmark machines. Torque (a) and power factor (b)

IV. Results

In this section the advantages and drawbacks of each model analyzed in this paper are presented and compared. The four models are:

- **Initial model**, marked in red. It is the starting model from [6], represented with (1) or (23) with $k_{sat} = 1$, $k_{cross,d} = 1$, $k_{crossq} = 1$.
- **Saturated model**, marked in greed. In this model, only the d-axis saturation kept into account. Represented with (23) with $k_{sat} > 1$, $k_{cross,d} = 1$, $k_{cross,q} = 1$.
- **FEAfix1 model**, marked in blue. In this model, both saturation and cross saturation are modeled with 1 FEA simulation. Represented with (23) with $k_{sat} > 1$, $k_{cross,d} < 1$, $k_{cross,q} < 1$.
- **FEAfix4 model**, marked in orange. In this model, both saturation and cross saturation are modeled with 4 FEA simulations. Represented with (23) with $k_{sat} > 1$, $k_{cross,d} < 1$, $k_{cross,q} < 1$.

First, a design example is presented, with the same benchmark machines introduced before. Than, a comprehensive comparison between the models is performed, dealing with precision and computational time aspects.

A. Case-study designs

A first comparison on the models is done on the three benchmark machines introduced in the second section. Each model estimation of each machine is compared with a FEA simulation, evaluated in the working point computed by the design process. This is important because the saturation factor change the d-axis current, changing the working point. Fig. 12 shows the torque (Fig. 12a) and power factor (Fig. 12b) of the three benchmark machines, estimated by the models (colored bars) and computed with FEA simulations (black transparent bars). The estimations of the initial model (red bars) are far from the FEA simulations: torque is overestimated of about 4-6 Nm (30% circa of the estimated torque), while the power factor is less overestimated, but the error is near 0.04. The saturation factor (green bars) heavily improve the torque forecast, thanks to the improvement on the λ_{md} estimation. The power factor is underestimate with this model, but the discrepancy between the analytical calculation and the FEA results is lower. The FEAfix procedures (FEAfix1 in blue and FEAfix4 in orange) solve definitively the estimation problem, eliminating the gap between the model and FEA results.

B. Comparison of accuracy and computational time

Dealing with the model comparison, an important term is the computational time needed to draw the xb-plane. The trade-off between the computational time and the model precision on the torque and power factor estimation is summarized in Fig. 13. The three plots compare the computational time (Fig. 13a), the mean torque error (Fig. 13b) and the mean power factor error (Fig. 13c) of the three benchmark machines designed with the four models previously analyzed. From this comparison is evident that the higher time consumption of the Saturated model is more than balanced by a dramatically higher precision on torque estimation, respect to the Initial model. Regarding the power factor, the benefit is present, but

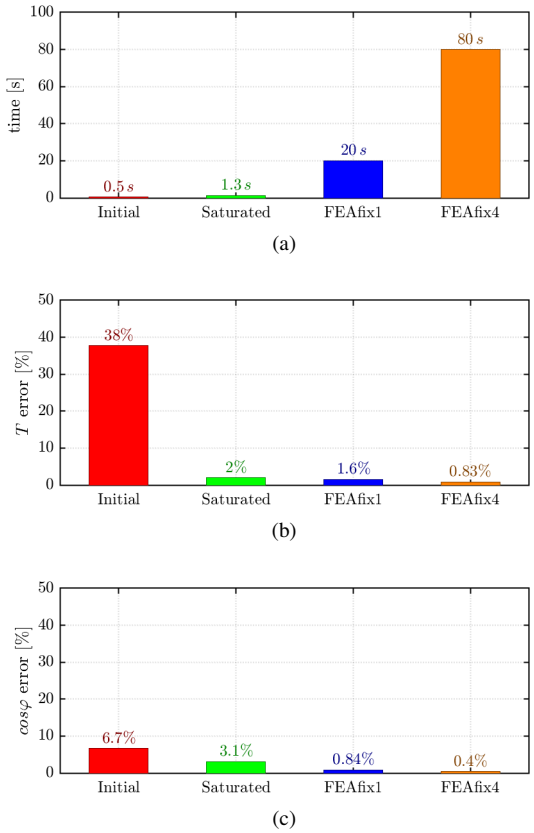

Fig. 13. Tradeoff between the behaviors of the four analyzed models. Computational time (a), mean torque error respect to FEA simulations (b) and mean power factor error respect to FEA simulations (c), following the designs of the previous section.

less evident than on torque. The FEAfix approach definitively solves the estimation problem, by cutting off the power factor error and still reducing the torque error. The cost of the higher precision is the computational time: one FEA simulation for the FEAfix procedure takes approximatively 20 s. This means that the FEAfix1 model takes less more than 20 seconds to be computed, while the FEAfix4 model can take up to 80 seconds.

V. Conclusion

In this paper, a fast approach to the SyR machine design is reviewed and its weak points are improved. The upgrades aim to increase the model accuracy without increasing the computational time and maintaining the generality of the analytical model. The first upgrade to the original model dealt with the iron saturation effect. An easy equation based on a simplified equivalent circuit was added increasing the performance estimation precision with no extra computational efforts. The second upgrade was the enhance of the analytical model with FEA simulations. This hybridized model, called FEAfix, uses selected FEA points to improve the output figures estimation of an extensive class of SyR machines. This strategy allows to remove the estimation errors, keeping the generality of the model and with a limited computational time growth. All the improvements are validated on a benchmark case using accurate FEA simulations. The FEA-augmented model is than included in SyR-e, an open-source framework for the electrical machine design, evaluation and optimization, enhancing the tool capability.

References

[1] A. Vagati, M. Pastorelli, G. Francheschini and S. C. Petrache, "Design of low-torque-ripple synchronous reluctance motors," in IEEE Transactions on Industry Applications, vol. 34, no. 4, pp. 758-765, Jul/Aug 1998.

[2] I. Boldea, "Reluctance synchronous machines and drives," Oxford University Press, vol. 34, no. 38, 1996.

[3] M. Degano, H. Mahmoud, N. Bianchi and C. Gerada, "Synchronous reluctance machine analytical model optimization and validation through finite element analysis," 2016 XXII International Conference on Electrical Machines (ICEM), Lausanne, 2016, pp. 585-591.

[4] F. Cupertino, G. Pellegrino and C. Gerada, "Design of Synchronous Reluctance Motors With Multiobjective Optimization Algorithms," in IEEE Transactions on Industry Applications, vol. 50, no. 6, pp. 3617-3627, Nov.-Dec. 2014.

[5] Y. Wang, D. M. Ionel, M. Jiang and S. Stretz, "Large scale optimization of electronically controlled synchronous reluctance machines using CE-FEA and differential evolution," 2015 IEEE International Electric Machines and Drives Conference (IEMDC), Coeur d'Alene, ID, 2015, pp. 1702-1708.

[6] I.Boldea, T.Fukao, T.A.Lipo, L.Malesani, T.J.E.Miller, A.Vagati, "Synchronous Reluctance Motors and Drives: a new alternative ", Tutorial Course at IEEE-IAS 94 Meeting., Section 3.

[7] D. A. Staton, T. J. E. Miller and S. E. Wood, "Maximising the saliency ratio of the synchronous reluctance motor," in IEE Proceedings B - Electric Power Applications, vol. 140, no. 4, pp. 249-259, July 1993.

[8] G. Pellegrino, P. Guglielmi, A. Vagati and F. Villata, "Core Losses and Torque Ripple in IPM Machines: Dedicated Modeling and Design Tradeoff," in IEEE Transactions on Industry Applications, vol. 46, no. 6, pp. 2381-2391, Nov.-Dec. 2010.

[9] M. Gamba, G. Pellegrino and F. Cupertino, "Optimal number of rotor parameters for the automatic design of Synchronous Reluctance machines," 2014 International Conference on Electrical Machines (ICEM), Berlin, 2014, pp. 1334-1340.

[10] C. Bianchini, M. Davoli, G. Pellegrino, F. Immovilli and E. Lorenzani, "Low cost PM synchronous servo-applications employing asynchronous-motor frame," 2015 IEEE Energy Conversion Congress and Exposition (ECCE), Montreal, QC, 2015, pp. 6090-6095.

[11] F. Cupertino, G. Pellegrino et al., "SyR-e: Synchronous Reluctance (machines) - evolution" Internet: https://sourceforge.net/projects/syr-e/. [Mar. 29, 2018]